

# Modified virtual synchronous generator based-primary frequency regulation for renewable generation integrated into power system

Zhengyang Hu<sup>1</sup>, Bingtuan Gao<sup>1</sup> ✉, Ning Chen<sup>2</sup>, Linan Qu<sup>2</sup>, Chenyu Peng<sup>1</sup>

<sup>1</sup>School of Electrical Engineering, Southeast University, Nanjing 210096, People's Republic of China

<sup>2</sup>State Key Laboratory of Operation and Control of Renewable Energy & Storage Systems, China Electric Power Research Institute, Nanjing 210003, People's Republic of China

✉ E-mail: gaobingtuan@seu.edu.cn

ISSN 1751-8687

Received on 17th August 2019

Revised 18th February 2020

Accepted on 29th June 2020

doi: 10.1049/iet-gtd.2019.1271

www.ietdl.org

**Abstract:** To guarantee the frequency stability of renewable energy sources (RESs) generation integrated into the power system, primary frequency regulation (PFR) for RES generation controlled by virtual synchronous generator (VSG) has been concerned extensively. This study mainly focuses on the dynamic and steady-state characteristics of VSG in the PFR dead-band. Based on the typical structure of VSG, small-signal model of the conventional VSG is established to analyse the issue of the sharp change of angular frequency. Consequently, a novel modified VSG (M-VSG) controller is proposed, which can ensure a stable angular frequency and synchronise with the grid without the phase-locked-loop. The inertia and damping properties of M-VSG are studied theoretically by eigenvalue analysis, and the design procedure of control parameters is presented. To enhance the practicability, a flexible PFR strategy of M-VSG is added considering inertia mode, bidirectional mode, and unidirectional mode according to the operation state of RES generation. Moreover, after PFR is added, the proposed controller is analysed with eigenvalue loci to guarantee the stability and dynamic characteristics outside the dead-band. Finally, hardware-in-the-loop experiment results based on RT-LAB demonstrate the validity of the theoretical analysis and the superiority of M-VSG in participating in flexible PFR.

## Nomenclature

$D_p$	virtual damping coefficient
$D_q$	voltage droop coefficient
$E$	root-mean-square (RMS) value of internal potential
$f_n$	the nominal value of grid frequency
$f_d$	the dead-band frequency
$K_{fil}, T_{fil}$	gain and time constant of high pass filter
$k_p^*$	PFR slope coefficient of M-VSG
$P_{ref}$	reference value of active power
$P_e$	output active power
$P_{load}$	active power consumed by system load
$P_{PFR}^*$	per unit value of active power reference of PFR
$P_{max}^*, P_{min}^*$	upper and lower limits of $P_{PFR}^*$
$Q_{ref}$	reference value of reactive power
$Q_e$	output reactive power
$T_{JVSG}$	inertia time constant
$T_K$	time constant of the reactive power loop
$U_{pcc}$	RMS value of the phase voltage of the point of common coupling (PCC)
$U_0$	rated RMS value of the phase voltage of the PCC
$X_S$	impedance of the filter reactor
$\delta_{VSG}$	phase difference between the internal potential and voltage of the PCC
$\omega_{VSG}$	virtual angular frequency
$\omega_0$	rated angular frequency
$\omega_g$	grid voltage angular frequency
$\omega_d^*$	per unit value of damped oscillation frequency of VSG
$\Delta\omega^*$	per unit value of difference between the virtual angular frequency of M-VSG and the nominal value
$\theta_{VSG}$	internal potential phase of VSG

## 1 Introduction

To solve the energy shortage and environmental issues, more and more renewable energy sources (RESs) are being integrated into power system [1–3]. However, RES generation operates decoupled from the power system, resulting in the decreasing of equivalent inertia and frequency regulation capacity in the power system. With the increasing penetration of RES generation, the frequency stability of power system has become a serious problem, which requires RES generation to participate in primary frequency regulation (PFR) and provide inertial support similar to synchronous generators (SGs) [4–6]. Therefore, it is of great theoretical and practical value to study the control strategy of RES generation when integrated into the power system.

Converters are the key devices for RES generation to be integrated into the power system, which include the input-side converter and the grid-side converter [7]. The control strategy of the input-side converter varies from a different type of RES, but the grid-side converter can be controlled in the same way [8]. A grid-side converter can be controlled as a current source [9–11] or a voltage source [12–17]. When controlled as a current source, the converter is difficult to provide frequency and voltage support. Hence, this paper focuses on the latter.

The VSG, which represents the voltage source converter control strategy, was proposed to mimic both the steady-state characteristics and the dynamic characteristics of an SG [12–16]. The virtual synchronous generator (VSG) control generates amplitude, frequency, and phase angle for its terminal voltage based on its power command, ensuring the ability to contribute to the regulation of grid voltage and frequency [17]. The VSG used in [12, 15] ( $\omega_0$ -VSG) can participate in PFR and increase the equivalent inertia of the system, but the slope coefficient of PFR is coupled to the damping coefficient since the frequency reference equals the nominal value, resulting in the design difficulties of the slope coefficient of PFR. When the frequency deviates from the nominal value, the output active power of VSG will also deviate due to the damping characteristics of VSG, unless the damping coefficient equals to 0 [18, 19]. However, if the damping

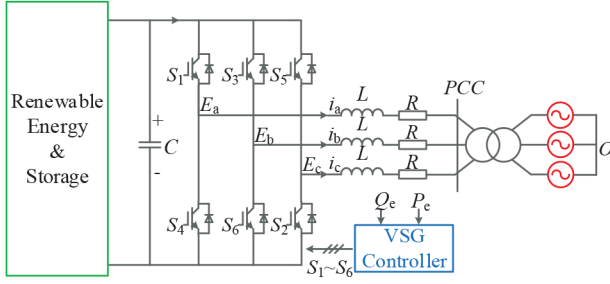


Fig. 1 Typical structure of VSG

coefficient is 0, the damping ratio of the VSG will equal to 0 [20], which could drive the control system to be unstable. Thus, the PFR dead-band cannot be set in  $\omega_b$ -VSG. In the traditional power system, the purpose of setting dead-bands is to reduce excessive governor activities and turbine mechanical wear [21, 22]. As for RES generation, PFR dead-bands are used to avoid the extreme actions of the PFR caused by small random frequency variations during normal operation conditions [23, 24]. The other widely-used VSG was studied in [16, 25] ( $\omega_g$ -VSG), which uses the grid frequency as the reference value. This kind of VSG mimics the damping effect of SG better, and separates the PFR with the damping effect of VSG, which means that the inertial support and the steady-state output active power can be controlled respectively. However, the grid frequency signal must be achieved by a phase-locked-loop (PLL) which is inherently non-linear, complex and difficult to tune the parameters [14, 26]. Furthermore, when the load power has a step change, there always exists obvious angular frequency changes in this VSG [27], affecting the power system frequency stability.

In this paper, the dynamic properties of the  $\omega_g$ -VSG are analysed based on the single-machine infinite bus system integrated with RES generation, and an M-VSG controller is proposed. The main contribution of this paper includes the following: (i) based on the small-signal model, the principle of the virtual angular frequency spike in  $\omega_g$ -VSG is explained theoretically; (ii) based on the transfer function of the active power loop in  $\omega_g$ -VSG, the M-VSG is proposed for providing a smooth virtual angular frequency and participating in the PFR with dead-band; (iii) the steady-state and dynamic characteristics of M-VSG are analysed by automatic control theory and eigenvalue analysis, and the design procedure of control parameters is presented; (iv) according to the operation state of RES generation, a flexible PFR strategy is proposed considering different ranges of dead-bands.

The rest of the paper is organised as follows. In Section 2, the mathematical model of  $\omega_g$ -VSG is presented and the stability of virtual angular frequency of  $\omega_g$ -VSG is analysed theoretically. In Section 3, a novel M-VSG control is proposed, and the design process of control parameters is given. In Section 4, a flexible PFR of M-VSG with dead-band is proposed. Hardware-in-the-loop (HIL) experiments based on RT-LAB are performed in Section 5 to demonstrate the validity of the theoretical analysis and the effectiveness of M-VSG. Finally, the conclusions are presented in Section 6.

## 2 Conventional $\omega_g$ -VSG control analysis

The typical structure of the VSG applied to the renewable generation is shown in Fig. 1, which consists of the RES generation, storage system, converter, filter circuit, step-up transformer, and grid.

The control block diagram of conventional  $\omega_g$ -VSG is shown in Fig. 2, where the active power loop emulates the inertia, damping and PFR of SG to calculate the reference frequency and phase of the modulation wave, whereas the reactive power loop emulates the voltage regulation to calculate the amplitude of the modulation wave.

According to the control diagram shown in Fig. 2, the mathematical model of  $\omega_g$ -VSG in a per unit (p.u.) system can be

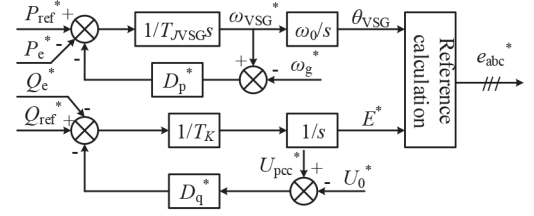


Fig. 2 Control block diagram of  $\omega_g$ -VSG

expressed as (1) when the transmission lines resistances are neglected

$$\begin{cases} \frac{d\theta_{VSG}}{dt} = \omega_{VSG}^* \omega_0 \\ T_{JVSG} \frac{d\omega_{VSG}^*}{dt} = P_{ref}^* - P_e^* - D_p^*(\omega_{VSG}^* - \omega_g^*) \\ T_K \frac{dE^*}{dt} = Q_{ref}^* - Q_e^* - D_q^*(U_{pcc}^* - U_0^*) \\ P_e^* = \frac{E^* U_{pcc}^*}{X_S} \sin \delta_{VSG} \\ Q_e^* = \frac{(E^* \cos \delta_{VSG} - U_{pcc}^*) U_{pcc}^*}{X_S} \end{cases} \quad (1)$$

All the variables superscripted with \* denote the p.u. value of the corresponding ones. Assuming  $E^*$  is constant [25], the small-signal mathematical model of the active power part of VSG can be deduced according to (1). The variables subscripted with 0 denote the steady value of the corresponding ones, shown in (2)

$$\begin{cases} T_{JVSG} \Delta \omega_{VSG}^* = \Delta P_{ref}^* - \Delta P_e^* - D_p^*(\Delta \omega_{VSG}^* - \Delta \omega_g^*) \\ \Delta P_e^* = \frac{E_0^* U_{pcc0}^* \cos \delta_{VSG0}}{X_S} \Delta \delta_{VSG} + \frac{E_0^* \sin \delta_{VSG0}}{X_S} \Delta U_{pcc}^* \\ + \frac{E_0^* \cos \delta_{VSG0}}{X_S} \Delta \delta_{VSG} \Delta U_{pcc}^* \end{cases} \quad (2)$$

Generally,  $\delta_{VSG0}$  is quite small due to the small impedance between the converter and PCC. Let  $\cos \delta_{VSG0} = 1$  and  $\sin \delta_{VSG0} \Delta U_{pcc}^* = 0$  [25]. Moreover, the second-order perturbation term in (2) can be neglected, and (2) can be rewritten as

$$\begin{cases} T_{JVSG} \Delta \omega_{VSG}^* = \Delta P_{ref}^* - \Delta P_e^* - D_p^*(\Delta \omega_{VSG}^* - \Delta \omega_g^*) \\ \Delta P_e^* = \frac{E_0^* U_{pcc}^*}{X_S} \Delta \delta_{VSG} \\ \Delta \delta_{VSG} = \frac{\omega_0}{s} (\Delta \omega_{VSG}^* - \Delta \omega_g^*) \end{cases} \quad (3)$$

Due to the power balance in power system,  $\Delta P_e^* = \Delta P_{load}^*$ . To study the dynamic characteristics of  $\omega_g$ -VSG in the PFR dead-band, the PFR is not covered in the control strategy shown in Fig. 2. The  $\omega_g$ -VSG autonomously provides dynamic inertial support without changing the  $P_{ref}$ . Thus,  $\Delta P_{ref}^* = 0$  when  $P_{load}^*$  changes. Let  $k_{VSG} = (\omega_0 E^* U_{pcc}^*) / X_S$ , and eliminate  $\omega_g^*$  from (3), so that

$$\frac{\Delta \omega_{VSG}^*}{\Delta P_{load}^*} = - \frac{D_p^* s + k_{VSG}}{T_{JVSG} k_{VSG} s} \quad (4)$$

Equation (4) is the transfer function of load power to the virtual angular frequency. According to the initial-value theorem, let  $s \rightarrow \infty$  in (4), and then the high-frequency gain of the transfer function can be deduced

$$\frac{\Delta \omega_{VSG}^*}{\Delta P_{load}^*}(0_+) = \lim_{s \rightarrow \infty} s \cdot \frac{1}{s} \cdot \left( - \frac{D_p^* s + k_{VSG}}{T_{JVSG} k_{VSG} s} \right) = - \frac{D_p^*}{T_{JVSG} k_{VSG}} \quad (5)$$

Equation (5) implies that the virtual angular frequency will mutate if the load power has a step change, which results from the large high-frequency gain, compromising the frequency stability of the power system.

To solve this problem and allow the converter to operate without PLLs, a novel controller is designed in the following section.

### 3 M-VSG controller design

#### 3.1 M-VSG control structure design

According to (4), the relationship between active power and virtual angular frequency can be obtained without  $\omega_g^*$  signal. Hence, if using the transfer function in (4) to substitute the inertia and damping part in  $\omega_g$ -VSG, PLLs are unnecessary for the M-VSG controller. The control block diagram of the active power loop in M-VSG is shown in Fig. 3. M-VSG has the same reactive power loop as  $\omega_g$ -VSG.

The expression of  $G_{P\omega}(s)$  in Fig. 3 can be designed as (6), with the same form as (4)

$$G_{P\omega}(s) = \frac{T_1 s + 1}{K_1 s}. \quad (6)$$

The small-signal model of the active power control loop in M-VSG controller can be simplified as Fig. 4.

According to (4)–(6), both the numerator and the denominator of  $G_{P\omega}(s)$  are first order, resulting in the large high-frequency gain. Therefore, to guarantee a smooth virtual angular frequency change when the load fluctuates, a pole should be added in  $G_{P\omega}(s)$ , as shown in (7)

$$G_{P\omega}(s) = \frac{T_1 s + 1}{K_1 s(T_2 s + 1)}. \quad (7)$$

Then, the open-loop transfer function of active power loop of M-VSG, the closed-loop transfer function of active power loop of M-VSG and the transfer function of frequency disturbance are derived as follows:

$$G_P(s) = G_{P\omega}(s) \cdot G_{\omega P}(s) = \frac{k_{VSG}(T_1 s + 1)}{K_1 s^2(T_2 s + 1)} \quad (8)$$

$$\Phi_P(s) = \frac{\Delta P_e^*}{\Delta P_{ref}^*} = \frac{k_{VSG}(T_1 s + 1)}{K_1 T_2 s^3 + K_1 s^2 + k_{VSG} T_1 s + k_{VSG}} \quad (9)$$

$$\Phi_{\omega P}(s) = \frac{\Delta P_e^*}{\Delta \omega_g^*} = \frac{k_{VSG} K_1 s(T_2 s + 1)}{K_1 T_2 s^3 + K_1 s^2 + k_{VSG} T_1 s + k_{VSG}}. \quad (10)$$

#### 3.2 M-VSG control parameter design and analysis

To design the control parameters of M-VSG controller, the relationship among inertia time constant, damping coefficient and  $K_1$ ,  $T_1$  and  $T_2$  need to be investigated and established. Referring to the traditional  $\omega_0$ -VSG control [12], the physical implication of each parameter can be clarified. The small-signal transfer function of the traditional  $\omega_0$ -VSG which mimics the second-order rotor motion equation of the SG is shown in Fig. 5 [15].

An inertia element and a differentiation element should be added in the damping feedback channel to achieve the transfer function shown in (8), which can be regarded as a high pass filter. The transfer function of the high pass filter can be written as follows:

$$G_{fil}(s) = \frac{K_{fil} s}{T_{fil} s + 1}. \quad (11)$$

To ensure  $D_p^*$  remains unchanged in the initial stage of the response, let  $G_{fil}(s)|_{s \rightarrow \infty} = 1$ , and (12) can be achieved

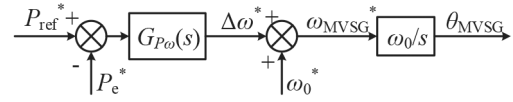


Fig. 3 Control block diagram of the active power loop in M-VSG

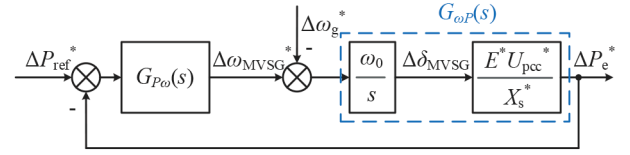


Fig. 4 Simplified small-signal transfer function of active power loop of M-VSG

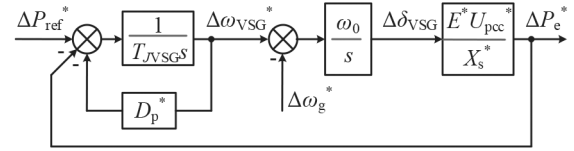


Fig. 5 Transfer function of active power loop of traditional  $\omega_0$ -VSG control

$$K_{fil} = T_{fil}. \quad (12)$$

The transfer function of  $\Delta \omega_{VSG}^*/(\Delta P_{ref}^* - \Delta P_e^*)$  can be obtained

$$\frac{\Delta \omega_{VSG}^*}{\Delta P_{ref}^* - \Delta P_e^*} = \frac{T_{fil} s + 1}{(T_{JVSG} + D_p^* T_{fil}) s (\frac{T_{JVSG} T_{fil}}{T_{JVSG} + D_p^* T_{fil}} s + 1)}. \quad (13)$$

According to (7) and (13), the control parameters  $K_1$ ,  $T_1$  and  $T_2$  can be expressed by  $T_{JVSG}$ ,  $D_p^*$  and  $T_{fil}$ , shown in (14)

$$\begin{cases} T_1 = T_{fil} \\ T_2 = \frac{T_{JVSG} T_{fil}}{T_{JVSG} + D_p^* T_{fil}} \\ K_1 = T_{JVSG} + D_p^* T_{fil} \end{cases} \quad (14)$$

Firstly, the value of  $T_{fil}$  can be confirmed by analysing the damping properties of SGs. The damping effect in SGs includes mechanical damping effect and electromagnetic damping effect. The mechanical friction causes the former, whereas the latter is caused by the induced current in the amortisseur winding. When the rotating speed of the rotor is equal to that of the magnetic field of the stator, there is no induced current in the amortisseur winding. If the load changes, the rotor will subject to unbalanced torques, resulting in a change of rotating speed. Then, a relative motion exists between the rotor and the magnetic field of the stator, and the amortisseur winding on the rotor produces induced current. This induced current produces a damping torque in the opposite direction to the relative motion of the rotor, which impedes the rotor speed change. Besides, the mechanical damping effect can be neglected since it is much less than the electromagnetic damping effect. According to the characteristics of the added high pass filter, the damping loop can work under dynamic conditions but is invalid in the steady-state. Therefore, the proposed M-VSG control mimics the electromagnetic damping effect, which means M-VSG can damp the dynamic change of virtual rotor speed but have no effect on the output active power in the steady-state. Generally, control systems are underdamping. If  $\omega_0$ -VSG control system is underdamping, the damped oscillation frequency can be calculated according to the second-order rotor motion equation as

$$\omega_d = \frac{\sqrt{4T_{JVSG}k_{VSG} - D_p^{*2}}}{2T_{JVSG}}. \quad (15)$$

To make sure that the high pass filter can damp the dynamic change of virtual rotor speed, the cutoff frequency of high pass

filter should be designed less than  $\omega_d^*$ . Additionally, if the cutoff frequency is too small, the rapidity of the damping part will be reduced [28], and the settling time for the controller will increase. Hence, let the cutoff frequency of high pass filter be equal to  $\omega_d^*/3$  to achieve both the rapidity and the effectiveness of the control system. According to the automatic control theory,  $T_{fil}$  is equal to the inverse of the cutoff frequency, which can be expressed as

$$T_{fil} = \frac{6T_{JVSG}}{\sqrt{4T_{JVSG}k_{VSG} - D_p^{*2}}} \cdot \quad (16)$$

Secondly, the value range of  $T_{JVSG}$  can be determined. The parameter  $T_{JVSG}$  represents the inertia time constant of M-VSG. The inertia time constant of an SG intends the time required for the rotor to be accelerated from static to nominal speed with the rated mechanical torque, with a range of 4–12 s [29]. Correspondingly, to make sure that M-VSG can provide the inertial support similar to SGs, the value range of  $T_{JVSG}$  is from 4 to 12s.

Thirdly, the eigenvalue analysis is used to investigate the effect of  $T_{JVSG}$  and  $D_p^*$ . According to (9), (14), and (16), the eigenvalue loci of the active power loop in M-VSG with different  $T_{JVSG}$  and increasing  $D_p^*$  can be obtained, and the damping ratio increases from 0 to 1, shown in Fig. 6. It can be observed that all three poles are on the left side of the imaginary axis, ensuring the stability of M-VSG control system. With  $T_{JVSG}$  increasing from 4 to 12, the poles shift to the right, reducing the stability of M-VSG control system. When  $T_{JVSG}$  is constant, the damping ratio of conjugate poles increases with  $D_p^*$  increasing, making the control system responds slower and enhancing the system stability meanwhile.

To directly observe the influence of the change of  $T_{JVSG}$  and  $D_p^*$  on the frequency response characteristics of M-VSG control system, the transfer function  $\Phi_{\omega P}(s)$  in (10) should be analysed. Fig. 7 is the step response curves of  $\Phi_{\omega P}(s)$ . The  $X_g^*$  is chosen as 0.189, while  $\omega_0$  is chosen as  $100\pi$ , which corresponds to the HIL experiment in Section 5. In the simulation,  $\omega_g$  drops by 0.1 Hz at 0.5 s. When  $\omega_g$  has a step change, M-VSG can provide the active power support similar to the inertial response of SGs. It is entirely different from the  $\omega_0$ -VSG since the inertial support and PFR are decoupled. As can be observed in Fig. 7, the variation of parameters can only affect the dynamic process, but the steady-state output always equals 0. Furthermore, as can be seen in Fig. 7a, increasing  $D_p^*$  causes a steadier step response curve. The peak value of the active power and the contribution to the frequency stability maintenance increase with  $D_p^*$  increasing. As is illustrated in Fig. 7b, increasing  $T_{JVSG}$  causes a more oscillating step response curve. The peak value of the active power and the contribution to the frequency stability maintenance increase with  $T_{JVSG}$  increasing.

Then, the characteristics of M-VSG controller to follow the active power reference value are analysed. According to (9), the unit step response of transfer function  $\Phi_P(s)$  with different  $T_{JVSG}$  can be obtained, shown in Fig. 8. Based on the analysis of parameters  $T_{JVSG}$  and  $D_p^*$  in M-VSG controller, taking the stability and rapidity of the control system into consideration, multiple sets of control parameters of M-VSG are chosen as an example, shown in Table 1. It should be noted that these combinations are not the only choices of control parameters. According to the automatic control theory, the damping ratio should be chosen between 0.4 and 0.8. The damping ratios of the parameters in Table 1 are selected at about 0.707, which is widely used in engineering. Based on the specific requirements of power system as well as the capacity of RES generation, the parameter selection is flexible.

As shown in Fig. 8, with the increase of  $T_{JVSG}$ , the settling time increases from 0.5 to 0.92 s. However, the influence of the change of  $T_{JVSG}$  on percent overshoots is not obvious, each of which is 34% approximately. From (9), it can be observed that there is a zero in the transfer function  $\Phi_P(s)$ , raising the overshoot of the system. Hence, to decrease the overshoot, the differentiation

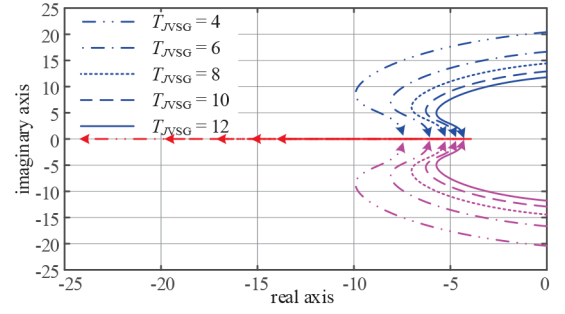


Fig. 6 Eigenvalue loci with different  $T_{JVSG}$  and increasing  $D_p^*$

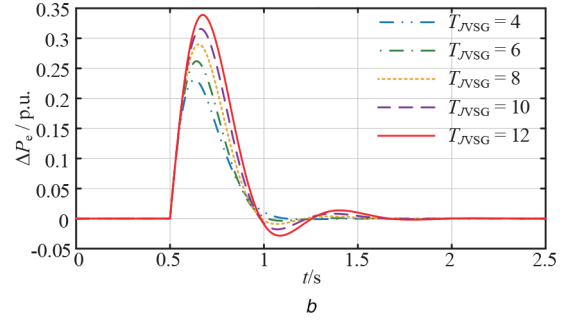
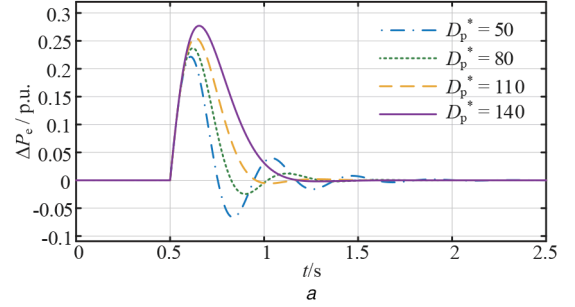


Fig. 7 Step response curves of  $\Phi_{\omega P}(s)$  with different (a)  $D_p^*$  when  $T_{JVSG} = 6$ , (b)  $T_{JVSG}$  when  $D_p^* = 120$

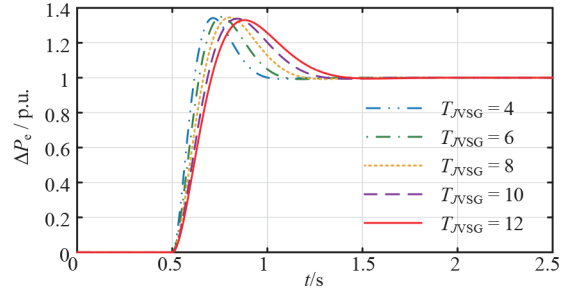


Fig. 8 Unit step response of transfer function  $\Phi_P(s)$  with different  $T_{JVSG}$

Table 1 Multiple sets of control parameters of M-VSG

$T_{JVSG}$ , s	4	6	8	10	12
$D_p^*$ , p.u.	100	120	140	160	180
$\zeta$	0.679	0.660	0.670	0.690	0.715

element in  $\Phi_P(s)$  is moved to the feedback channel, and the unit negative feedback control is turned to the speed negative feedback control, as shown in Fig. 9.

In Fig. 9,  $G_{P\omega}'(s)$  and the transfer function  $\Phi_P'(s)$  are deduced as follows:

$$G_{P\omega}'(s) = \frac{1}{K_1 s(T_2 s + 1)} \quad (17)$$



$$\Phi_P'(s) = \frac{\Delta P_e^*}{\Delta P_{\text{ref}}^*} = \frac{k_{\text{VSG}}}{K_1 T_2 s^3 + K_1 s^2 + k_{\text{VSG}} T_1 s + k_{\text{VSG}}}. \quad (18)$$

As is shown in Fig. 10, when the active power reference value has a unit step change, the output active power overshoot of M-VSG is reduced obviously and the settling time has a little decrease compared with the previous simulation shown in Fig. 8. The overshoots are almost equal to 0. Since the transfer function of  $\Delta P_e^*/\Delta \omega_g^*$  is still as shown in (10), the characteristics of the frequency response remain unchanged.

In summary, compared with the  $\omega_g$ -VSG control, PLLs are not required in M-VSG control, and the virtual angular frequency of M-VSG changes smoothly. M-VSG can provide inertial support for power system when the grid frequency varies, and the output active power equals its reference in the steady-state consistently even if the grid frequency deviates from the nominal value. Furthermore, the parameter design is flexible, enhancing the adaptation of M-VSG to different systems.

#### 4 PFR with dead-band for M-VSG

After analysing the PFR dead-band characteristics, PFR should be added in M-VSG control to complete the investigation. PFR is an important method of frequency regulation, but it responds slower than inertial response [29]. When the grid frequency deviation fluctuates in a tiny range, PFR can have a negative effect on frequency regulation [21]. Besides, when load power varies slightly, grid frequency can be maintained near the nominal value without PFR. Using PFR in this situation is a waste of frequency regulation resources. If the wind speed is limited or the weather is cloudy, and the output active power of RES generation such as wind or photovoltaic power generation is too low to take part in PFR, inertial support is required only. Moreover, if the full-load operation is carried by RES generation, it merely can reduce the output active power. In this situation, the unidirectional PFR is suitable for RES generation due to the lack of extra active power.

After separating PFR with the inertial response, the dead-band and slope of PFR can be designed individually, making RES generation more adaptable to different scenarios. The PFR block diagram is shown in Fig. 11.

According to different scenarios, three operation modes are set in Fig. 11. M-VSG operates in the inertia mode when switch  $S_2$  turns off. In this mode, M-VSG only provides inertial support for power system. When switch  $S_1$  is thrown at position 1 and switch  $S_2$  turns on, M-VSG operates in the bidirectional PFR mode. The bidirectional PFR dead-band is  $[f_n - f_d, f_n + f_d]$ . When switch  $S_1$  is thrown at position 2 and switch  $S_2$  turns on, M-VSG operates in the unidirectional PFR mode. The unidirectional PFR dead-band is  $(-\infty, f_n + f_d]$ .

If the output active power of RES generation controlled by M-VSG is equal to or less than 0.3 p.u., switch  $S_2$  turns off. Then, the inertia mode is used, and  $P_{\text{PFR}}^* = 0$ . It is worth mentioning that the value of switch signal which is 0.3 p.u. can be adjusted according to the actual situation such as the frequency regulation capacity estimation or the generator operation instructions. The value of the switch signal does not affect the characteristics of the controller in each mode.

When the output active power of RES generation controlled by M-VSG is more than 0.3 p.u., PFR is required and switch  $S_2$  turns on. In this case, if the full-load operation is taken by RES generation, switch  $S_1$  should be thrown at position 2 and unidirectional PFR mode is used. The  $P_{\text{PFR}}^*$  of M-VSG can be achieved as

$$P_{\text{PFR}}^* = \begin{cases} 0 & \Delta \omega^* \leq f_d^* \\ -k_p^* \times (\Delta \omega^* - f_d^*) & \Delta \omega^* > f_d^* \end{cases}. \quad (19)$$

Bidirectional PFR mode should be used if the deloading operation is taken by RES generation. Switch  $S_1$  is thrown at position 1 and  $P_{\text{PFR}}^*$  can be derived as

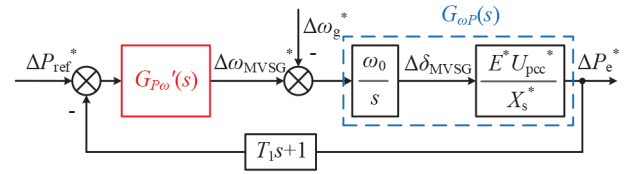


Fig. 9 Simplified small-signal model of active power loop of M-VSG

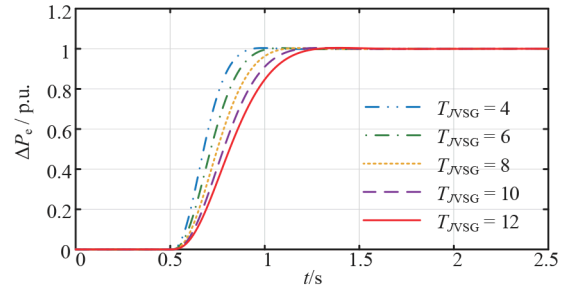


Fig. 10 Unit step response of transfer function  $\Phi_P'(s)$  with different  $T_{JVSG}$

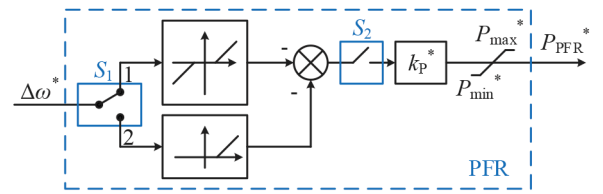


Fig. 11 PFR block diagram

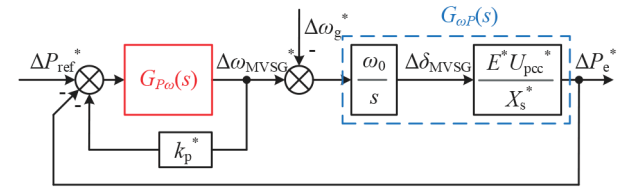


Fig. 12 Small-signal transfer function of active power loop of M-VSG with PFR

$$P_{\text{PFR}}^* = \begin{cases} -k_p^* \times (\Delta \omega^* + f_d^*) & \Delta \omega^* < -f_d^* \\ 0 & -f_d^* \leq \Delta \omega^* \leq f_d^* \\ -k_p^* \times (\Delta \omega^* - f_d^*) & \Delta \omega^* > f_d^* \end{cases}. \quad (20)$$

The small-signal stability and characteristics of M-VSG inside the dead-band is analysed in Section 3. After added the PFR strategy in M-VSG, the stability and characteristics should be studied when it is outside the dead-band. The small-signal model of active power loop of M-VSG with PFR is shown in Fig. 12.

Similar to (8) and (10), the open-loop and the closed-loop transfer function of active power loop of M-VSG with PFR are deduced as follows:

$$G_P''(s) = \frac{k_{\text{VSG}}(T_1 s + 1)}{K_1 T_2 s^3 + (K_1 + T_1 k_p^*) s^2 + k_p^* s} \quad (21)$$

$$\Phi_P''(s) = \frac{\Delta P_e^*}{\Delta P_{\text{ref}}^*} = \frac{k_{\text{VSG}}(T_1 s + 1)}{K_1 T_2 s^3 + (K_1 + T_1 k_p^*) s^2 + (k_p^* + k_{\text{VSG}} T_1) s + k_{\text{VSG}}}. \quad (22)$$

Referring to the PFR slope coefficient of SGs,  $k_p^*$  is set to 50. It means that each change of 1 Hz in frequency corresponds to 1 p.u. change of active power. Based on (22), the eigenvalue loci of the active power loop in M-VSG with PFR with different  $T_{JVSG}$  and increasing  $D_p^*$  can be obtained, and the damping ratio increases from 0 to 1, shown in Fig. 13.

From the eigenvalue loci, we can find that all three poles are on the left side of the imaginary axis, and the system stability is

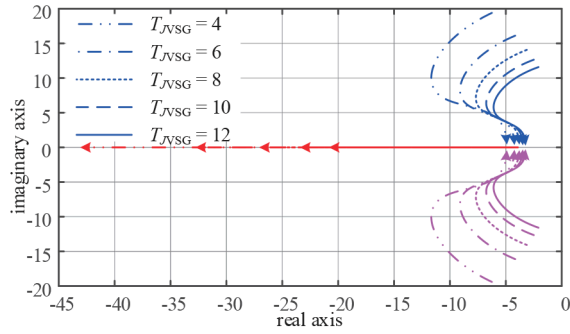


**Fig. 13** Eigenvalue loci with different  $T_{JVSG}$ , increasing  $D_p^*$ , and PFR added

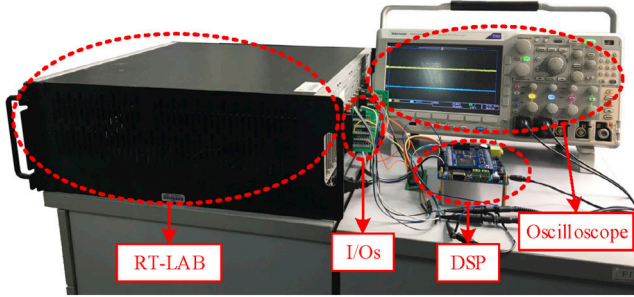


**Fig. 14** HIL experiment platform

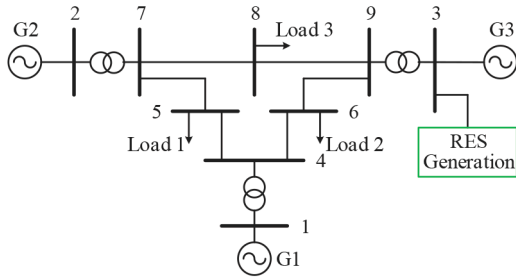


**Fig. 15** WSCC 3-machine 9-bus power system with RES generation integrated at bus 3

**Table 2** Electrical parameters of the RES power plant and control parameters of M-VSG

Parameters	Value	Parameters	Value
Nominal power, MVA	20	$U_{dc}$ , kV	30
Nominal AC line voltage, kV	13.8	$Q_{ref}$ , p.u.	0
Switching frequency, kHz	2	$X_s^*$ , p.u.	0.189
$T_{JVSG}$ , s	6	$k_p^*$ , p.u.	50
$D_p^*$ , p.u.	120	$f_d$ , Hz	0.06
$T_K$ , s	1.5	$P_{max}^*$ , p.u.	0.1
$D_q^*$ , p.u.	20	$P_{min}^*$ , p.u.	-0.1

guaranteed. Additionally, compared with M-VSG without PFR shown in Fig. 6, the damping ratio is increased when  $D_p^*=0$  due to the added PFR control. It can be calculated that the damping ratio of M-VSG change to 0.793, 0.797, 0.798, 0.798, 0.800, respectively under the control parameters shown in Table 1, meeting the requirement of automatic control theory.

## 5 HIL experiment results

To verify the validity of the theoretical analysis and the effectiveness of M-VSG, HIL experiments based on RT-LAB OP5600 are carried out. Fig. 14 shows the HIL experiment platform. An RES power plant integrated into the WSCC 3-machine 9-bus system shown in Fig. 15 is simulated by the RT-LAB real-time simulator. The RT-LAB simulator is provided with

the inputs and outputs which ensure the ability to interface with the DSP TMS320F28335 controller. The control strategy of the grid-side converter in RES power plant is accomplished in the DSP controller.

In Fig. 15, the RES generation is considered similar to the infinite bus system integration shown in Fig. 1. The nominal value of grid frequency is 50 Hz. The PFR dead-band frequency of SGs is 0.033 Hz, which is the typical value of thermal power generators in China. The other parameters of the system can be found in [30, 31]. The key parameters of RES power plant and M-VSG are listed in Table 2.

### 5.1 HIL experiment when grid frequency is in the dead-band

In order to analyse the operation properties of M-VSG when the frequency is in the dead-band, the scenario of slight load fluctuation in the power system is imitated. The load power of load 3 at bus 8 has a  $-2.5$  MW step change at 0.5 s. Then, the load power has a 5 MW step change at 1 s and has a  $-5$  MW step change at 2 s. When  $t = 3$  s, the load power has a 2.5 MW step change. The active power reference of M-VSG is 0.9 p.u.. The output active power, virtual angular frequency, and grid frequency waveforms with M-VSG,  $\omega_g$ -VSG, and  $\omega_0$ -VSG are shown in Fig. 16.

As illustrated in Fig. 16, after integrated into the power system, M-VSG can provide inertial support to power system when the load power fluctuates. Similar to the inertial response of SGs, M-VSG increases the output active power if grid frequency is decreasing and vice versa, which could reduce the rate of change of frequency (ROCOF) and enhance the equivalent inertia of power system. When the grid frequency remains unchanged in the dead-band, the output active power of M-VSG will follow the reference value. Fig. 16a shows that  $\omega_g$ -VSG can provide inertial support and follow the active power reference in the steady-state. However, as can be seen in Fig. 16b, the initial ROCOF of  $\omega_g$ -VSG is too large, verifying the theoretical analysis shown in (5). The virtual angular frequency of M-VSG changes smoothly, which is beneficial to the frequency stability of the power system. In addition, as the frequency reference of  $\omega_g$ -VSG, the output grid frequency of the PLL in Fig. 16c has a poor quality when the load changes. As for  $\omega_0$ -VSG, since the PFR is coupled to the damping effect if the load power is equal to the input power of generators,  $\omega_0$ -VSG will not achieve the steady-state until the frequency is adjusted to the nominal value. As shown in Fig. 16b, the virtual angular frequency of  $\omega_0$ -VSG is stable at about 1 p.u. finally. When  $t = 2$  s, the load power has already smaller than the input power of generators, but the grid frequency is still lower than the nominal value. The PFR response depends on the value of frequency, whereas the inertial response is dependent on the direction of frequency change. Hence,  $\omega_0$ -VSG responds slower than M-VSG, and the PFR has a negative effect in this situation. Therefore, when the grid frequency fluctuates near the nominal value, PFR is needless and a waste of frequency regulation resources, demonstrating the practicality of the proposed M-VSG controller and the PFR with dead-band.

### 5.2 HIL experiment when grid frequency is beyond the dead-band

**5.2.1 Bidirectional PFR:** To analyse the operation properties of M-VSG when the frequency is beyond the dead-band, the scenario of heavy load fluctuation in power system is imitated. The load power of load 3 at bus 8 has a  $-20$  MW step change at 0.5 s and then has a 40 MW step change when  $t = 2$  s. The active power reference of M-VSG is 0.9 p.u.. The output active power and virtual angular frequency waveforms with M-VSG,  $\omega_g$ -VSG, and  $\omega_0$ -VSG are shown in Fig. 17. The switch  $S_1$  in PFR is thrown at position 1.

As can be seen in Figs. 17a and b, M-VSG can provide dynamic inertial support as well as sustained active power support to power system. If the grid frequency is lower than the lower limit of the dead-band, M-VSG will participate in PFR and vice versa. Fig. 17a shows that the output active power of  $\omega_g$ -VSG in the

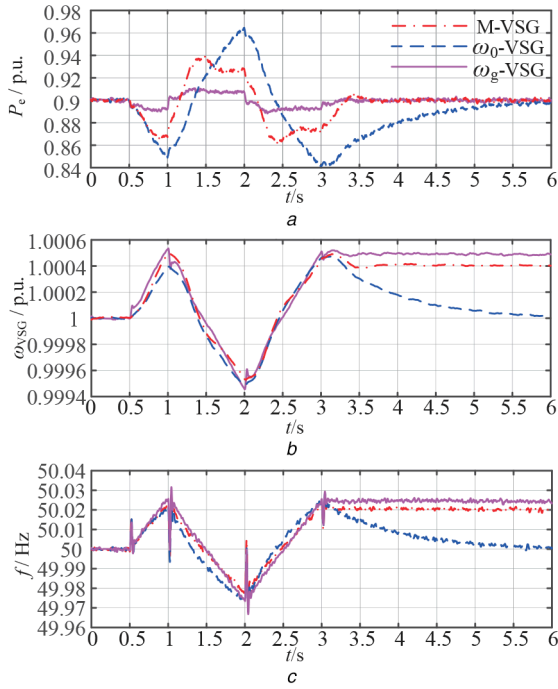


**Fig. 16** Waveform of  
(a) Output active power, (b) Virtual angular frequency, (c) Grid frequency with different controllers when load power fluctuates slightly

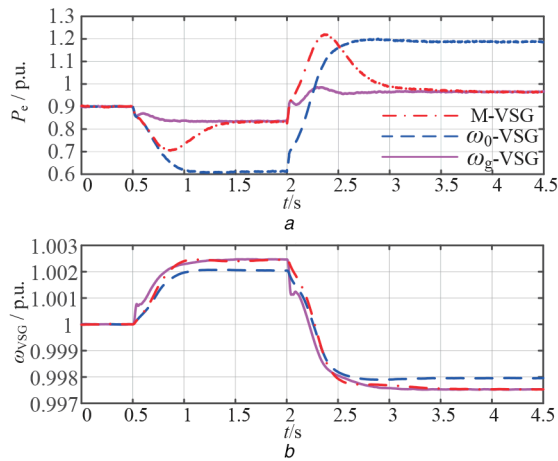


**Fig. 17** Waveform of  
(a) Output active power, (b) Virtual angular frequency with different controllers when load power fluctuates heavily

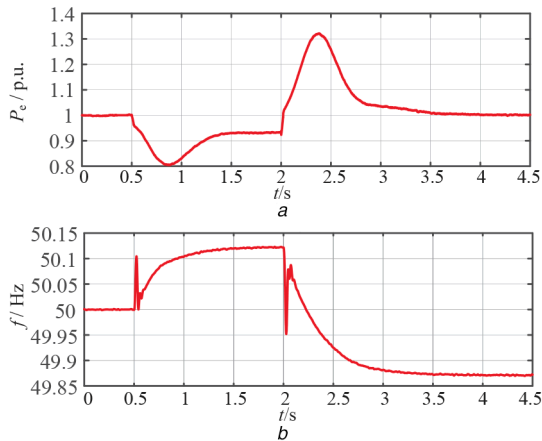


**Fig. 18** Waveform of  
(a) Output active power, (b) Grid frequency with M-VSG control when load power fluctuates heavily

steady-state is equal to that of M-VSG. However, comparing Fig. 17b with Fig. 16b, it can be observed that the more the load power changes, the more obvious the virtual angular frequency of  $\omega_g$ -VSG shifts in the initial stage. As illustrated in Figs. 17a and b, the output active power of  $\omega_0$ -VSG is 1.187 p.u. when the virtual angular frequency deviation of  $\omega_0$ -VSG equals 0.0021 p.u., corresponding to 0.105 Hz. Since the slope of PFR is coupled to the damping coefficient which is strongly related to the dynamic properties and damping ratio of  $\omega_0$ -VSG, the slope of PFR cannot be designed individually. It is unsafe for RES generation to output active power over the rated value. Thus,  $\omega_0$ -VSG has its limitation in frequency regulation. According to Sections 3 and 4, the peak value of the inertial support of M-VSG and the slope of PFR can be adjusted by changing the control parameters. Therefore, the flexibility and practicality of M-VSG are better than  $\omega_0$ -VSG.

**5.2.2 Unidirectional PFR:** When switch  $S_1$  in PFR is thrown at position 2, the unidirectional PFR mode is taken. The simulation scenario is consistent with that in bidirectional PFR, and the active power reference is 1 p.u.. The output of active power and grid frequency waveforms with M-VSG control is shown in Fig. 18. Since the  $\omega_0$ -VSG cannot realise unidirectional PFR and the disadvantages of the  $\omega_g$ -VSG have been analysed above, we only investigate the feasibility of M-VSG in this part.

As shown in Fig. 18, the load 3 has a  $-20$  MW step change at 0.5 s and the output active power of M-VSG drops rapidly, which is the inertial support. When  $t = 1.5$  s, the output active power is 0.932 p.u., lower than the reference value, which represents M-VSG is participating in the PFR. Similarly, M-VSG provides inertial support to the power system at 2 s, but the output active power drops to the reference value at 4 s, which represents M-VSG does not participate in PFR when the frequency is lower than the nominal value, demonstrating the effectiveness of M-VSG and unidirectional PFR strategy.

### 5.3 Stability verification after short circuit fault

To further verify the stability of the proposed controller, it is necessary to study its performance during and after short circuit fault conditions in WSCC 3-machine 9-bus power system shown in Fig. 15. In the test system, single-phase and three-phase short circuit faults on bus 5 are set. The faults occur when  $t = 0.5$  s and last for 0.1 s. The output active power, voltage and current of M-VSG waveforms under two different scenarios are shown in Figs. 19 and 20.

As can be seen in Fig. 19, the voltage of phase A drops to 0 during phase A short circuit fault, and recovers after the fault removal. The output active power cannot follow the power reference during the short circuit fault, and converges after a transient oscillation at 3 s. Since this paper mainly focuses on the dynamic and steady-state characteristics of VSG in the PFR dead-band, the fault current suppression should be studied in future work. The short circuit current grows very large at the moment the single-phase short circuit fault occurs.

From Fig. 20, it can be illustrated that the three-phase voltages of M-VSG drops to 0 during the three-phase short circuit fault, and recovers after removing the fault. The output active power drops to 0 due to the 0 voltage, and get back to the steady-state after a transient process. Similar to the single-phase short circuit fault scenario, the fault current also has a rapid rise at 0.5s.

In conclusion, the stability of the proposed controller and the power system can be guaranteed. The proposed controller oscillates during the transient process and converges in a few seconds.

## 6 Conclusions

In this paper, two commonly used VSG control strategies are studied by modelling and theoretical analysis. Based on the analysis results and automatic control theory, an M-VSG controller is proposed to overcome the defects of traditional VSG controllers. Four main conclusions can be drawn:



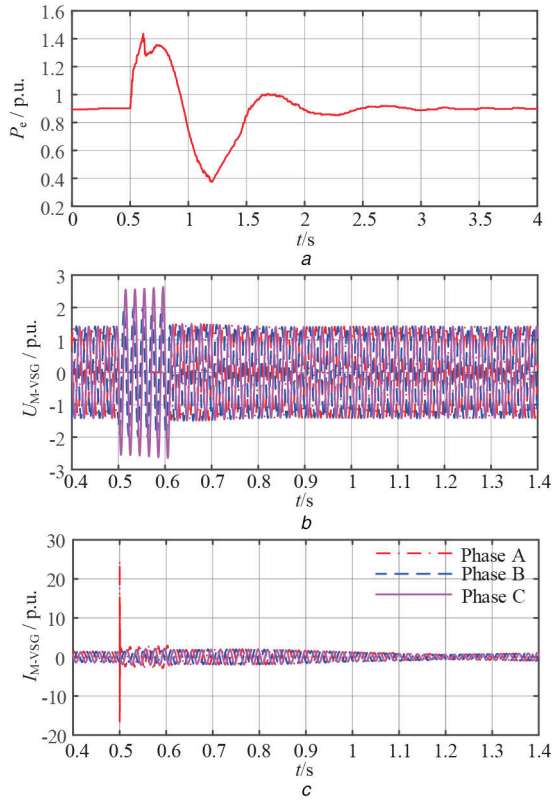


**Fig. 19** Waveform of  
(a) Output active power, (b) Voltage, (c) Current of M-VSG when single-phase short circuit fault occurs on bus 5

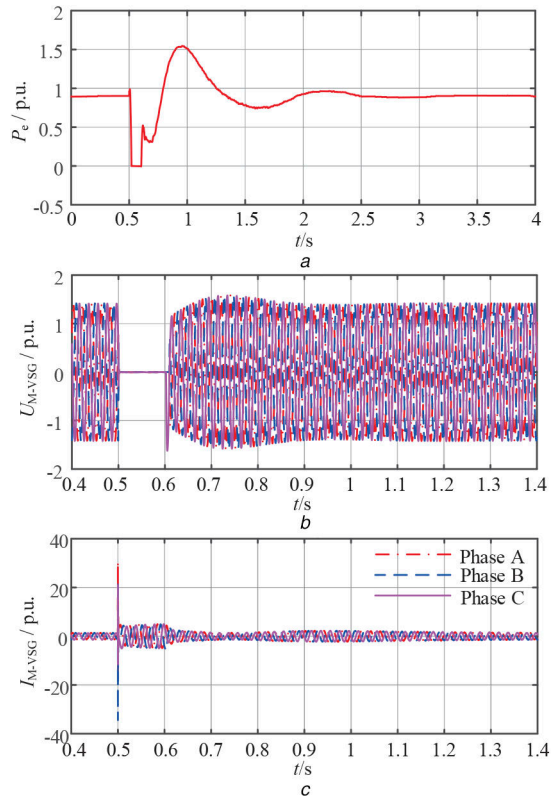


**Fig. 20** Waveform of  
(a) Output active power, (b) Voltage, (c) Current of M-VSG when three-phase short circuit fault occurs on bus 5

- (1) Due to the significant initial gain, the virtual angular frequency of  $\omega_g$ -VSG will mutate when the load power has a step change.
- (2) Compared with  $\omega_g$ -VSG, the proposed M-VSG can ensure a smaller initial ROCOF and synchronise with the grid frequency

without PLLs. Compared with  $\omega_0$ -VSG, the proposed M-VSG decouples PFR from the inertial support and can participate in PFR with dead-band.

(3) The parameter design of M-VSG is flexible, enhancing the adaptation of M-VSG to different systems. With  $T_{JVSG}$  increasing, the stability of M-VSG control system is reduced, and the peak value of the active power output when the grid frequency changes are improved. With  $D_p^*$  increasing, the control system responds slower, and the system stability will be enhanced. Meanwhile, the peak value of the active power output and the contribution to the frequency stability maintenance when the grid frequency changes are strengthened.

(4) The proposed M-VSG can participate in three different modes of PFR according to its working conditions. The dead-band and slope parameters of three PFR modes can be designed individually. The small-signal stability and dynamic characteristics of M-VSG with PFR are still desirable.

(5) The proposed M-VSG can be converged after the short circuit fault. The research on the fault current suppression can be studied in the future if possible.

## 7 References

- [1] Remon, D., Canizares, C.A., Rodriguez, P.: 'Impact of 100-MW-scale PV plants with synchronous power controllers on power system stability in northern Chile', *IET Gener. Transm. Distrib.*, 2017, **11**, (11), pp. 2958–2964
- [2] Serban, E., Ordonez, M., Pondiche, C.: 'Voltage and frequency grid support strategies beyond standards', *IEEE Trans. Power Electron.*, 2016, **32**, (1), pp. 298–309
- [3] Wang, S., Tomovic, K.: 'A novel active power control framework for wind turbine generators to improve frequency response', *IEEE Trans. Power Syst.*, 2018, **33**, (6), pp. 6579–6589
- [4] De Almeida, R.G., Pecos Lopes, J.A.: 'Participation of doubly fed induction wind generators in system frequency regulation', *IEEE Trans. Power Syst.*, 2007, **22**, (3), pp. 944–950
- [5] Pandey, S.K., Mohanty, S.R., Kishor, N.: 'A literature survey on load frequency control for conventional and distribution generation power systems', *Renew. Sustain. Energy Rev.*, 2013, **25**, pp. 318–334
- [6] Wang, Z., Wu, W.: 'Coordinated control method for DFIG-based wind farm to provide primary frequency regulation service', *IEEE Trans. Power Syst.*, 2017, **33**, (3), pp. 2644–2659
- [7] Chau, T.K., Yu, S.S., Fernando, T.L., et al.: 'A novel control strategy of DFIG wind turbines in complex power systems for enhancement of primary frequency response and LFO', *IEEE Trans. Power Syst.*, 2017, **33**, (2), pp. 1811–1823
- [8] Blaabjerg, F., Teodorescu, R., Liserre, M., et al.: 'Overview of control and grid synchronization for distributed power generation systems', *IEEE Trans. Ind. Electron.*, 2006, **53**, (5), pp. 1398–1409
- [9] Hwang, M., Muljadi, E., Jang, G., et al.: 'Disturbance-adaptive short-term frequency support of a DFIG associated with the variable gain based on the ROCOF and rotor speed', *IEEE Trans. Power Syst.*, 2016, **32**, (3), pp. 1873–1881
- [10] Attya, A.B., Anaya-Lara, O., Leithead, W.E.: 'Novel concept of renewables association with synchronous generation for enhancing the provision of ancillary services', *Appl. Energy*, 2018, **229**, pp. 1035–1047
- [11] Beck, H.P., Hesse, R.: 'Virtual synchronous machine'. 2007 9th Int. Conf. on Electrical Power Quality and Utilisation, Barcelona, Spain, 2007, pp. 1–6
- [12] Zhong, Q.C., Weiss, G.: 'Synchronverters: inverters that mimic synchronous generators', *IEEE Trans. Ind. Electron.*, 2010, **58**, (4), pp. 1259–1267
- [13] Zheng, T., Chen, L., Guo, Y., et al.: 'Comprehensive control strategy of virtual synchronous generator under unbalanced voltage conditions', *IET Gener. Transm. Distrib.*, 2017, **12**, (7), pp. 1621–1630
- [14] Zhong, Q.C., Nguyen, P.L., Ma, Z., et al.: 'Self-synchronized synchronverters: inverters without a dedicated synchronization unit', *IEEE Trans. Power Electron.*, 2013, **29**, (2), pp. 617–630
- [15] Gao, B., Xia, C., Chen, N., et al.: 'Virtual synchronous generator based auxiliary damping control design for the power system with renewable generation', *Energies*, 2017, **10**, (8), p. 1146
- [16] Shintai, T., Miura, Y., Ise, T.: 'Oscillation damping of a distributed generator using a virtual synchronous generator', *IEEE Trans. Power Deliv.*, 2014, **29**, (2), pp. 668–676
- [17] Alipoor, J., Miura, Y., Ise, T.: 'Power system stabilization using virtual synchronous generator with alternating moment of inertia', *IEEE J. Emerg. Sel. Top. Power Electron.*, 2015, **3**, (2), pp. 451–458
- [18] Zhong, Q.C., Ma, Z., Ming, W.L., et al.: 'Grid-friendly wind power systems based on the synchronverter technology', *Energy Convers. Manage.*, 2015, **89**, pp. 719–726
- [19] Ashabani, M., Mohamed, A.R.I.: 'Novel comprehensive control framework for incorporating VSCs to smart power grids using bidirectional synchronous-VSC', *IEEE Trans. Power Syst.*, 2014, **29**, (2), pp. 943–957
- [20] Wang, F., Zhang, L., Feng, X., et al.: 'An adaptive control strategy for virtual synchronous generator', *IEEE Trans. Ind. Appl.*, 2018, **54**, (5), pp. 5124–5133



- [21] Kou, G., Markham, P., Hadley, S., *et al.*: 'Impact of governor deadband on frequency response of the U.S. eastern interconnection', *IEEE Trans. Smart Grid*, 2016, **7**, (3), pp. 1368–1377
- [22] Bhui, P., Senroy, N., Singh, A.K., *et al.*: 'Estimation of inherent governor dead-band and regulation using unscented Kalman filter', *IEEE Trans. Power Syst.*, 2017, **33**, (4), pp. 3546–3558
- [23] Liu, Y., You, S., Liu, Y.: 'Study of wind and PV frequency control in US power grids EI and TI case studies', *IEEE Power Energy Technol. Syst. J.*, 2017, **4**, (3), pp. 65–73
- [24] Knap, V., Chaudhary, S.K., Stroe, D.I., *et al.*: 'Sizing of an energy storage system for grid inertial response and primary frequency reserve', *IEEE Trans. Power Syst.*, 2016, **31**, (5), pp. 3447–3456
- [25] Liu, J., Miura, Y., Ise, T.: 'Comparison of dynamic characteristics between virtual synchronous generator and droop control in inverter-based distributed generators', *IEEE Trans. Power Electron.*, 2016, **31**, (5), pp. 3600–3611
- [26] Harnefors, L., Bongiorno, M., Lundberg, S.: 'Input-admittance calculation and shaping for controlled voltage-source converters', *IEEE Trans. Ind. Electron.*, 2007, **54**, (6), pp. 3323–3334
- [27] Meng, X., Liu, J., Liu, Z.: 'A generalized droop control for grid-supporting inverter based on comparison between traditional droop control and virtual synchronous generator control', *IEEE Trans. Power Electron.*, 2018, **34**, (6), pp. 5416–5438
- [28] Hu, S.: '*Automatic control theory*' (China Science Publishing & Media Ltd, Beijing, 2013, 6th edn.)
- [29] Kundur, P., Balu, N.J., Lauby, M.G.: '*Power system stability and control*' (McGraw-hill, New York, 1994)
- [30] Sauer, P.W., Pai, M.A.: '*Power system dynamics and stability*' (Prentice-Hall, Upper Saddle River, NJ, 1998)
- [31] Prajapat, G.P., Senroy, N., Kar, I.N.: 'Stability enhancement of DFIG-based wind turbine system through linear quadratic regulator', *IET. Gener. Transm. Distrib.*, 2018, **12**, (6), pp. 1331–1338